A novel approach to modeling spacecraft spectral reflectance

Alexander Willison [*], Donald Bédard

Space Surveillance Research Laboratory, Department of Physics, Royal Military College of Canada, Kingston, ON, Canada

Abstract

Simulated spectrometric observations of unresolved resident space objects are required for the interpretation of quantities measured by optical telescopes. This allows for their characterization as part of regular space surveillance activity. A peer-reviewed spacecraft reflectance model is necessary to help improve the understanding of characterization measurements. With this objective in mind, a novel approach to model spacecraft spectral reflectance as an overall spectral bidirectional reflectance distribution function (sBRDF) is presented. A spacecraft's overall sBRDF is determined using its triangular-faceted computer-aided design (CAD) model and the empirical sBRDF of its homogeneous materials. The CAD model is used to determine the proportional contribution of each homogeneous material to the overall reflectance. Each empirical sBRDF is contained in look-up tables developed from measurements made over a range of illumination and reflection geometries using simple interpolation and extrapolation techniques. A demonstration of the spacecraft reflectance model is provided through simulation of an optical ground truth characterization using the Canadian Advanced Nanospace eXperiment-1 Engineering Model nanosatellite as the subject. Validation of the reflectance model is achieved through a qualitative comparison of simulated and measured quantities.

© 2016 COSPAR. Published by Elsevier Ltd. All rights reserved.

1. Introduction

The need for satellites by modern society is increasing the number of artificial resident space objects (RSOs) in Earth orbit (NASA Orbital Debris Program Office, 2014). The importance of space surveillance, defined as the "routine, operational service of detection, correlation, characterization, and orbit determination of space objects" (del Monte, 2007) is also increasing. This is required to manage these valuable space assets and to identify potential hazards and threats to humans on Earth and in orbit.

It is common for spacecraft, regardless of their orbital regime, to be beyond the diffraction-limitations of ground-based optical telescopes tasked for space surveillance. Typically on the order of 1 m, these telescopes are unable to obtain any useful spatial resolution in images (Luu et al., 2003). An example of an observation made using such a telescope is shown in Fig. 1, which contains four geostationary Earth orbit (GEO) satellites. These appear as spatially-unresolved point sources indistinguishable from one another.

Characterization is the practice of learning more about an object's nature in order to distinguish it from others. Characteristics of RSOs include: orientation, rate of change of orientation, physical shape, and surface material composition. Research into the determination of spacecraft characteristics using unresolved observations has focused on the analysis of light curves obtained by photometry (Luu et al., 2003; Scott et al., 2008; Somers, 2011; Bédard, 2013; Jolley, 2014). A broadband photometric light curve is a plot of the magnitude of spacecraft

* Corresponding author.
E-mail address: aawillison@gmail.com (A. Willison).

Fig. 1. An image containing Anik-F1, -F1R, -G1, and Echostar 17 (Jolley, 2014).

brightness, essentially a photon count, as a function of time. Photometric variation has been used successfully to determine the spin rate and spin axis of uncontrolled spacecraft (Somers, 2011), as well as to differentiate between co-located satellites in the GEO ring (Scott et al., 2008).

The light gathered by optical space surveillance sensors is reflected sunlight with spectral characteristics modified by the spacecraft's surface materials. Spectrometric variation is a change in spectral energy distribution (SED) as a function of time, orientation, or both, and is indicative of the surface composition of the object. Broadband photometric light curves do not indicate spectrometric variation while color-filtered light curves (products of color photometry) provide insight into the spectral changes occurring within the spacecraft's reflection over time (Bédard, 2013; Jolley, 2014; Bédard et al., 2014). These are produced by filtering the spacecraft-reflected photons over specific wavelength ranges. Unfortunately, while ideal for the surface composition characterization of unresolved objects, measurements of wavelength-resolved spectra are difficult to obtain due to changes in spacecraft illumination and reflection geometry coupled with the limited size of space surveillance-tasked telescopes. This results in poor signal-to-noise ratios for these measurements (Bédard et al., 2011). Regardless, numerous studies have been conducted to determine the utility of reflectance spectra for unresolved spacecraft characterization (Luu et al., 2003; Abercromby et al., 2006; Duggin et al., 2008; Hall, 2010; Chaudhary et al., 2011; Bédard and Lévesque, 2014). While none of these studies have demonstrated a marked level of success by conclusively determining a spacecraft's physical shape or material composition (or both) solely through the use of spectrometric measurements, they have provided

some insight into required *a priori* knowledge to differentiate one spacecraft from another.

The optical ground truth characterization of a spacecraft, hereafter referred to as its *ground truth*, is the collection of such *a priori* knowledge including physical dimensions, material composition, and the reflectance properties of these materials (Abercromby et al., 2006). This characterization is obtained in a laboratory and can be photometric or spectrometric in nature (Abercromby et al., 2006; Bédard and Lévesque, 2014). It serves as a basis to which all photometric and spectrometric measurements of the spacecraft in Earth orbit can be compared (Bédard et al., 2011).

The method to obtain a spacecraft's ground truth is to illuminate it with a collimated light source and take measurements using a far-field camera or spectrometer (Bédard and Lévesque, 2014). Performed in a controlled environment, this allows for the closest re-creation of the conditions under which the spacecraft will be illuminated and observed while in Earth orbit. The Canadian Advanced Nanospace eXperiment (CanX)-1 Engineering Model (EM) is a mock-up of the first spacecraft of the first Canadian picosatellite program (Wells et al., 2002). Bédard and Lévesque (2014) conducted an optical ground truth characterization experiment with this spacecraft, measuring its reflectance factor and bidirectional reflectance distribution function for two illumination and reflection geometry scenarios. At the conclusion of this experiment, Bédard et al. (2011) highlighted three challenges that this method presents:

1. Measurements must be made for as many different orientations as possible to reproduce the expected illumination and observation geometries in orbit.
2. Larger spacecraft are more difficult to illuminate uniformly with a collimated light source and observe with a far-field detector.
3. Access to a subject prior to launch can be difficult to obtain, especially for extended periods of time.

The reflectance of a spacecraft is a combination of the reflectance of its composite materials, with contributions proportional to their relative abundance (Luu et al., 2003; Hall, 2010). A method to simulate the ground truth of a spacecraft, thereby avoiding the disadvantages of a laboratory characterization, requires the spacecraft's computer-aided design (CAD) model and homogeneous samples of its composite materials. Application of the material reflectance characteristics to the CAD model results in a simulated spacecraft ground truth (Abercromby et al., 2006). This method avoids the difficulties of the laboratory characterization as small material samples can be manipulated easily, illuminated uniformly with a collimated light source, observed with a far-field sensor, and obtained for analysis with unimpeded access.

Current space-surveillance ability limits surface composition characterization to the interpretation of photometric

measurements. Accurate modeling is therefore required to produce synthetic spectrometric observations that can be used for interpretation, allowing for the characterization of unresolved objects.

1.1. The spectral bidirectional reflectance distribution function

The bidirectional reflectance distribution function is defined by Nicodemus et al. (1977) as "the ratio of the reflected radiance from a surface in a given direction to the incident radiance from a given direction, as a function of wavelength per unit steradian". Schaepman-Strub et al. (2006) introduced the term *spectral* bidirectional reflectance distribution function (sBRDF) to highlight its dependency on wavelength, λ, emphasizing that it is a spectrometric quantity. The sBRDF is a function of the six angles (Nicodemus et al., 1977) shown in Fig. 2. Illumination angles are denoted by subscript i and reflection angles are denoted by subscript r. θ_i and θ_r are the polar angles measured from the surface normal vector, $\vec{N}$, to the illumination and reflection vectors, $\vec{v}_i$ and $\vec{v}_r$, respectively. ϕ_i and ϕ_r are the azimuth angles measured from an arbitrary axis in the surface plane, usually defined by the illumination vector (Bass et al., 2010), though this is not the case depicted. Finally, ω_i and ω_r are the solid angles of the illumination source and reflection beam. This relationship is provided in Eq. (1) (Nicodemus et al., 1977; Schaepman-Strub et al., 2006):

$$f_r(\theta_i, \phi_i; \theta_r, \phi_r; \lambda) = \frac{dL_r(E_i; \theta_i, \phi_i; \theta_r, \phi_r; \lambda)}{L_i(\theta_i, \phi_i; \lambda) \cdot \cos\theta_i \cdot d\omega_i} \quad [\text{sr}^{-1}] \quad (1)$$

where $f_r(\theta_i, \phi_i; \theta_r, \phi_r; \lambda)$ is the sBRDF and L_i and L_r are the incident and reflected radiance, respectively. An example of a material sBRDF for several illumination and reflection geometries is provided in Fig. 3.
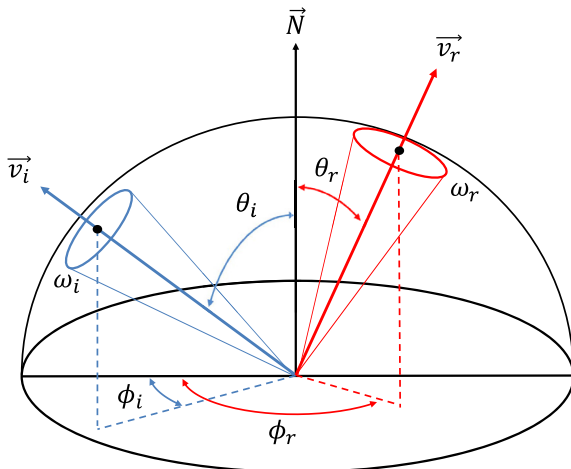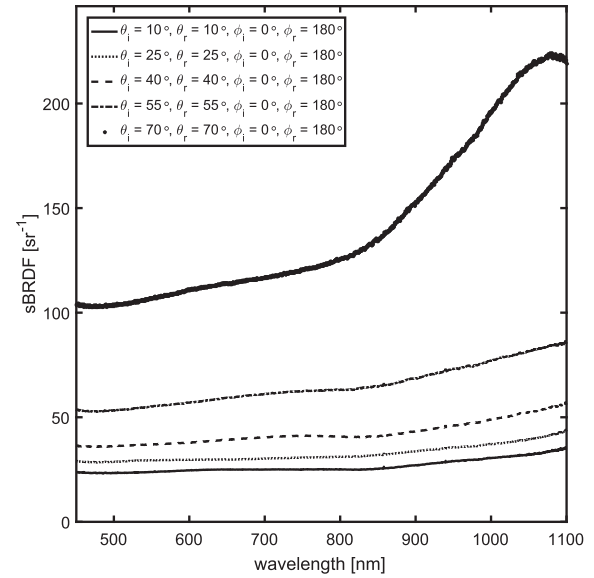

Fig. 3. The sBRDF of aluminum 6061-T6 for five illumination and reflection geometries, collected using the goniospectrometer constructed by Bédard et al. (2015).

1.2. The broadband bidirectional reflectance distribution function

The broadband bidirectional reflectance distribution function (BRDF), a term first used by Bédard et al. (2015), is an integration of the sBRDF over a wavelength range, thereby making it a photometric quantity. Eq. (2) provides the relationship between the BRDF and sBRDF (Bédard et al., 2015):

$$f_r(\theta_i, \phi_i; \theta_r, \phi_r) = \int_{\lambda_1}^{\lambda_2} f_r(\theta_i, \phi_i; \theta_r, \phi_r; \lambda) \cdot d\lambda \quad [\text{sr}^{-1}] \quad (2)$$

where $f_r(\theta_i, \phi_i; \theta_r, \phi_r)$ is the BRDF.

The term "BRDF" has been used in many ways by different authors, often with confusion. Bédard et al. (2015) established the naming convention of *spectral* and *broadband* BRDF to promote their differentiation. In keeping with this convention, the spectral BRDF is denoted as sBRDF and the broadband BRDF simply as BRDF for the remainder of this paper.

1.3. Previous work

Two developed products that model spacecraft spectral reflectance and are referenced in published literature are the Time-domain Analysis Simulation for Advanced Tracking (TASAT) system, and the Digital Imaging and Remote Sensing laboratory's Image Generation (DIRSIG) system. TASAT was designed at the U.S. Air Force Research Laboratory to simulate tracking and imaging systems to assess system performance and design (Riker et al., 1992). DIRSIG was developed at the Center for Imaging Science to produce radiometric images that are spectral in nature with radiance ranging from the visible to long infra-red (Schott et al., 1999). Both TASAT and DIRSIG

Fig. 2. The illumination and reflection geometry of an infinitesimal area, defined by its surface normal vector.

are unavailable in the public domain, leaving the validity of their modeling approaches in question as they have not been subjected to peer review. As the authors could not assess the strengths and weaknesses of these software products directly, their validity was inferred through published details of their inputs and products.

TASAT is a modular set of routines that model ground-based and space-based optical systems. It considers the relative geometry between the illumination source, target, and observer, as well as the absolute radiometry, atmospheric effects, and sensor capabilities (Duggin et al., 2008). TASAT is capable of producing physically-accurate images of complicated subjects, such as spacecraft, using their CAD models and the BRDFs of their surface materials. Two notable uses of this product are presented here: the first by Luu et al. (2003) to generate spacecraft reflectance spectra, and the second by Hall et al. (2012) for the identification of spacecraft materials from unresolved spectra.

The TASAT satellite materials database was referenced as a source of material BRDFs in both publications. Some examples of the contents of this database were provided by Hall et al. (2012), who depicted the BRDF of LORD Aeroglaze® A276 white paint and aluminum 5457-H116 for a wavelength of 600 nm at a single undefined illumination angle. Data pertaining to the total number of wavelengths, and illumination and reflection geometries contained within the TASAT material BRDF database was not provided. The hemispherical reflectance of these materials was shown for a wavelength range between 400 nm and 1200 nm. These included discontinuities whose presence suggests incomplete reflectance data, though they were unexplained by the author. Based on this evidence, there is indication that the TASAT material BRDF database is not complete, and raises questions concerning the validity of TASAT-simulated quantities.

Hall mentioned that the measurements contained within the database were fit to the Beard-Maxwell theoretical BRDF model, implying that this was a requirement for their use. This model was intended to specifically simulate painted surfaces by considering the combined contribution of a specular component produced by a top layer (the paint), and a subsurface scattering component of the material below (Maxwell et al., 1973). Reasoning for its use with aluminum 5457-H116, which is not a painted surface, was not provided. The Beard-Maxwell BRDF model is known to decrease in accuracy for materials that are more specular (Duggin et al., 2008) due to a subsurface scattering component (Maxwell et al., 1973), though the point at which this model breaks from measured results could not be found in published literature. It is unclear how many BRDF measurements the BRDF model was fitted to. The requirement for fitting the measurements contained in the TASAT material BRDF database to a theoretical model provides further confirmation that it is incomplete.

Luu et al. (2003) measured the reflectance spectrum of the Galaxy V spacecraft seven times over the course of one evening and compared simulated TASAT spectra for the same scenario. The measured Galaxy V reflectance spectra varied over time, with some observations exhibiting spectral features that were absent in others; however, the TASAT-simulated spectra were devoid of these features. No quantitative analysis was provided, and a qualitative analysis was difficult due to differences in the presentation of results. That said, there was little variation between individual simulated spectra, notably due to the absence of differentiating spectral features. In fact, the spectra were so similar that it was difficult to tell that seven were presented in the same figure. Based on these results, it is clear that the reflectance quantity produced by TASAT did not vary with changes in spacecraft orientation, implying that the material spectral reflectance was not a function of illumination and observation geometry. Specifically, BRDF, and therefore sBRDF, intensities did not vary nor did spectral features shift with changes in geometry, as was demonstrated by Bédard et al. (2015). Fig. 3 portrays the variation in sBRDF intensity with changes in geometry for aluminum 6061-T6; it should be noted, however, that the absorption feature at about 800 nm does not shift. Bédard et al. (2015) did show that the spectral features of triple-junction photovoltaic (TJPV) cells shift with changes in geometry, and attributed this phenomenon to thin-film interference. Conversely, while the TASAT results presented by Hall et al. (2012) indicated that the relationship between spectral reflectance and geometry was considered, the simulated spacecraft reflectance spectra possessed low fidelity, leaving uncertainty about the precise behavior of spectral features.

Based on the analysis of published details of the inputs and products of TASAT, the inferred weaknesses of the system are its spacecraft material BRDF database, which appears to be incomplete, and its use of theoretical BRDF models, which are not capable of accurately representing all material types. The fact that not all TASAT-simulated spacecraft reflectance quantities change with variations in illumination and reflection geometry also raises concerns about the accuracy of the system.

DIRSIG is a collection of data input files and sub-models originally designed to simulate remote-sensing imagery, emphasizing the inclusion of radiometric processes that affect spectral image formation. It is capable of rendering images of arbitrarily complicated surface shapes, such as CAD models, provided the BRDF of their surface materials.

An example of modeling spacecraft reflectance using DIRSIG was recently published by Bennett et al. (2014). Material BRDFs were empirically fitted to the Ward (Ward, 1992) empirical BRDF model. This model was developed to be used to describe reflectance measured by a gonioreflectometer, a photometric device, and is wavelength-independent. Bennett et al. (2014) presented the measured BRDF of multiple materials as a function of degrees-off-specular, along with their fitted Ward BRDF, though the model did not appear to accurately represent the measured BRDF of some materials, specifically

the solar cell. Bennett et al. (2014) indicated that in order to better represent material reflectance they "are working toward using [BRDF] measurements directly without having to use a fit model", though further details were not provided. It is unclear how DIRSIG is able to employ the wavelength-independent Ward BRDF to model spectral reflectance of spacecraft, which was shown by Bédard et al. (2015) to be wavelength-dependent.

The use of DIRSIG by Bennett et al. (2014) provided radiometric images of a spacecraft, although it is unclear whether spectra could be produced by the system in its current form; none were presented as a product of the simulation. This lack of simulated spectra, combined with DIRSIG's use of wavelength-independent BRDF models, leaves the system's quantitative accuracy in question.

1.4. This work

A spacecraft reflectance model that is available in the public domain and has been validated through peer-review is necessary to help improve the understanding of characterization measurements for space surveillance. The following research has been conducted with this overarching goal in mind.

A novel approach to use *a priori* knowledge of a spacecraft's physical characteristics and material composition to model its spectral reflectance, effectively simulating its optical ground truth characterization, is presented. Spacecraft spectral reflectance is modeled in two ways: first by measuring the sBRDF of homogeneous spacecraft materials for a range of illumination and reflection geometries, and developing an extended empirical sBRDF database using simple interpolation and extrapolation techniques, thereby avoiding the use of BRDF models while simultaneously maintaining physically-accurate reflectance characteristics; and second, through the use of triangular-faceted CAD models to determine the proportional contribution of each homogeneous material to the overall spacecraft sBRDF. This approach not only permits the simulation of quantities that are measured by optical telescopes, such as photometric light curves, it enables the analysis of the underlying spectrometric data. This allows for the interpretation of the surface composition of unresolved objects for space surveillance characterization.

A demonstration of spacecraft spectral reflectance model is provided through simulation of an optical ground truth characterization. Such an experiment was conducted by Bédard and Lévesque (2014) using the CanX-1 EM nanosatellite as the subject. Validation of the reflectance model is achieved through a qualitative comparison of simulated and measured quantities.

2. Aim and objectives

The aim of this research was to develop an approach to model the spectral reflectance of a spacecraft as an overall sBRDF. This would be accomplished by determining the sBRDF of each homogeneous material on the spacecraft through the illumination and reflection geometry of its respective facets, and calculating the contribution of each material to the total reflectance. The following objectives were established to achieve this goal:

1. Measure the sBRDF of homogeneous spacecraft materials for a range of illumination and reflection geometries.
2. Develop empirical sBRDF look-up tables for all illumination and reflection geometries from measurements.
3. Develop a scheme to mathematically represent complex spacecraft with multiple surface materials.
4. Derive an algorithm to calculate the overall sBRDF of a spacecraft.

The success of the experiment would be assessed by simulating quantities equivalent to those measured by Bédard and Lévesque (2014) during the CanX-1 EM optical characterization experiment. Specifically, this would be performed through qualitative comparison of:

1. The simulated sBRDF of the +X side of the CanX-1 EM and the measured reflectance factor.
2. The simulated BRDF of the CanX-1 EM and the measured photometric light curve.

Comparison of simulated and measured quantities is qualitative as they are not equivalent: the sBRDF and reflectance factor, while both spectral in nature, are different quantities, as are the BRDF and photometric light curves. That being said, the sBRDF and reflectance factor are both spectral quantities whose features are expected to be similar, while photometric light curves are products of the BRDF and should demonstrate similar behaviors.

3. Modeling spacecraft spectral reflectance

This section outlines the approach to model spacecraft spectral reflectance using empirical sBRDF data. It begins by describing how the sBRDF of homogeneous spacecraft materials was measured for a range of illumination and reflection geometries, followed by the method to develop empirical look-up tables from these measurements. Next, the mathematical representation scheme by which spacecraft, composed of multiple materials and possessing complex surface features, is provided. The section concludes by deriving an algorithm to calculate a spacecraft's overall sBRDF, considering its illumination and reflection geometry, as well as the proportional contribution of its component materials.

3.1. Measuring the sBRDF of homogeneous spacecraft materials for a range of illumination and reflection geometries

The illumination and reflection geometry presented in Fig. 2 was modified to enable simple measurement

acquisition and to streamline the development of empirical look-up tables. This modified geometry, shown in Fig. 4, references the "illumination plane", the plane defined by the illumination and surface normal vectors, $\vec{v}_i$ and $\vec{N}$, respectively. The specular reflection vector, $\vec{v}_s$, and the projection of the reflection vector onto the illumination plane, $\vec{v}_{r,proj}$ are also critical. The three key angles of this geometric system are the illumination polar angle, θ_i, the "difference-in-polar" angle, $\Delta\theta$, and the "from-illumination-plane" angle, ϕ. The solid angles, ω_i and ω_r, are removed as the illumination source and reflection beam are considered points for this modification.

The "difference-in-polar" angle, $\Delta\theta$, is located between $\vec{v}_s$ and $\vec{v}_{r,proj}$: this angle is negative if it is on the $\vec{v}_i$ side of $\vec{v}_s$, as shown in Fig. 4, and positive if it is opposite. The "from-illumination-plane" angle, ϕ, is the angle located between $\vec{v}_r$ and the illumination plane. Regardless of which side of the illumination plane this angle is located on, it is positive. This makes the assumption that material reflectance is isotropic on either side of the illumination plane. This modification in the illumination and reflection geometry means that the sBRDF is now a function of these angles: $f_r(\theta_i; \Delta\theta; \phi; \lambda)$.

The sBRDF of each homogeneous spacecraft material was measured using the goniospectrometer constructed by Bédard et al. (2015), modified to obtain "from-illumina tion-plane" reflection geometries by mounting the sensor on a goniometer stage, as recommended by Willison (2015). Fig. 5 depicts the placement of this component within the overall system.

The sampling scheme to measure a material's sBRDF for multiple illumination and reflection geometries is shown in Fig. 6. It was developed following the sampling recommendations of Willison (2015), considering that the goniometer stage was manually operated: adequate
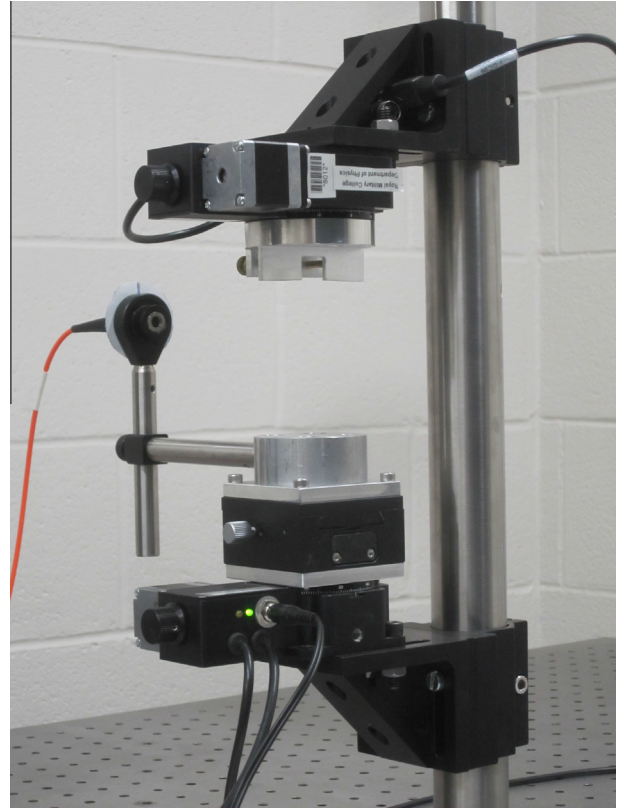

Fig. 5. The goniospectrometer sensor was mounted on a goniometer stage to obtain "from-illumination plane" reflection geometries that were unobtainable using the system originally constructed by Bédard et al. (2015).

sampling of the sBRDF would be achieved, while the amount of time and effort required to do so would be reduced. It is important to note that Fig. 6 depicts the positioning of a spectrometer's sensor within the reflection beam, not different points on the material sample within the illumination beam. The center of the sensor's field of view remains fixed on its point of rotation, located at the center of the illumination beam on the material sample.

The scheme is followed by fixing θ_i and changing the $\Delta\theta$ and ϕ values, achieving a total of 28 unique illumination
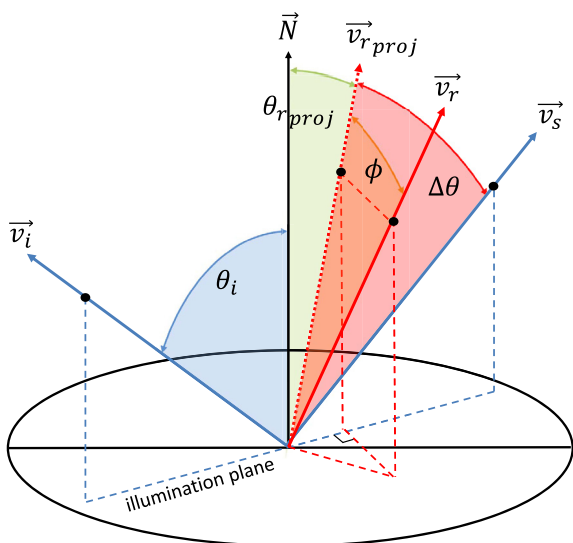

Fig. 4. The modified illumination and reflection geometry. Note that the $\Delta\theta$ shown is negative.
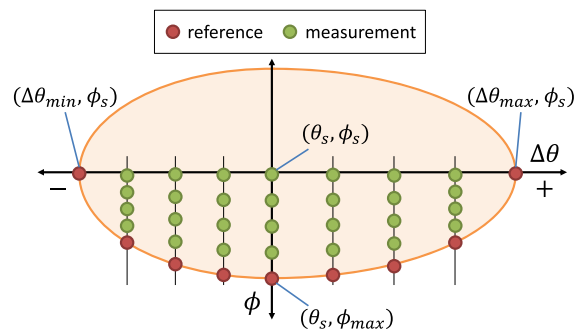

Fig. 6. The sampling scheme used to measure the experimental sBRDF for one θ_i value. The location of specular reflection, (θ_s, ϕ_s), and key reference points are indicated. Note that the reflection beam exhibits a difference in shape with respect to $\Delta\theta$ on opposite sides of specular.

and reflection geometries. The reference points are located where the reflectance becomes indistinguishable from noise and is therefore considered zero. This sampling scheme was observed for five θ_i values, resulting in a total of 112 sBRDF measurements taken per homogeneous spacecraft material, a number that is relatively low considering the infinite number of possible illumination and reflection geometries. A flow chart of the process to measure a material's sBRDF is provided in Fig. 7.

An example of the range of reflection geometries that results from using this sampling scheme is provided in Table 1: in this case, aluminum 6061-T6, for $\theta_i = 50°$. The measured BRDF associated with the illumination and reflection geometry range is shown in Fig. 8.

3.2. Developing empirical sBRDF look-up tables for all illumination and reflection geometries from measurements

The development of an empirical sBRDF look-up table that accurately represented material reflectance, from relatively few measurements, required the establishment of uniform illumination and reflection geometries to enable the use of simple interpolation and extrapolation methods.

First, the maximum ϕ_{max} used to measure the sBRDF of a material, $\phi_{max,material}$, between all θ_i values was determined. An array of 21 uniformly-spaced ϕ values was generated, where $d\phi = \phi_{max,material}/20$. This number was considered reasonable as it enabled angular fidelity while ensuring that resulting look-up tables were moderate in size. Linear interpolation established the spectral reflectance for all ϕ contained in this array, for each measured $\theta_i, \Delta\theta,$ and λ. In the case of aluminum 6061-T6, while ϕ_{max} in Table 1 was $2.1°, \phi_{max,material} = 2.5°$ at $\theta_i = 30°$. The linear interpolation occurred for all ϕ between $0°$ and $\phi_{max,material}$, where $d\phi = 1.25°$.

Next, the minimum $\Delta\theta_{min}$ and maximum $\Delta\theta_{max}$ used to measure the sBRDF of a material, $\Delta\theta_{min,material}$ and $\Delta\theta_{max,material}$, between all θ_i was determined. An array of 21 $\Delta\theta$ values was generated with $0°$ at the median, where $d\Delta\theta_{min} = \Delta\theta_{min,material}/10$ and $d\Delta\theta_{max} = \Delta\theta_{max,material}/10$. This treatment was required as the shape of the reflection beam could be different on opposite sides of specular with respect to $\Delta\theta$, as shown in Fig. 6. Linear interpolation established the spectral reflectance for all $\Delta\theta$ contained in this array, for each measured θ_i and λ, for all ϕ. The $\Delta\theta_{min,material}$ and $\Delta\theta_{max,material}$ of aluminum 6061-T6 were $-46°$ and $51°$, respectively, at $\theta_i = 30°$.

Finally, cubic smoothing splines were fitted to the sBRDF for each $\phi, \Delta\theta,$ and λ as functions of θ_i. These splines were used to interpolate and extrapolate the sBRDF for all integers between $0°$ and $90°$, inclusive. Fig. 9 presents the BRDF of aluminum 6061-T6 contained in the empirical look-up table resulting from the interpolation and extrapolation of the measured sBRDF for the same illumination and reflection geometry range as Fig. 8.
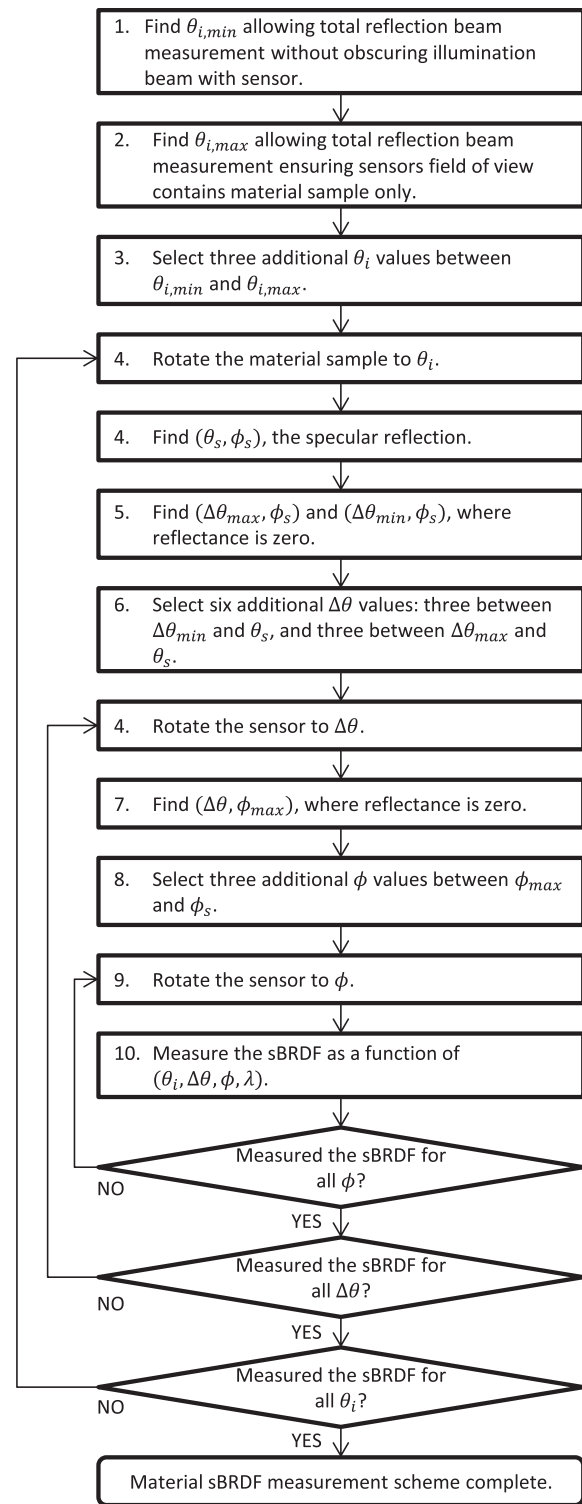

Fig. 7. A flow chart of the process to measure a material's sBRDF.

3.3. A scheme to mathematically represent complex spacecraft

Spacecraft are represented using triangular-faceted computer-aided design (CAD) models based on the STereoLithography (STL) format, where matrices define

Table 1
The reflection geometries used to measure the sBRDF of aluminum 6061-T6, for $\theta_i = 50°$. Reference angles, where no sBRDF measurement was made, are shaded.

		ϕ_s	ϕ_1	ϕ_2	ϕ_3	ϕ_{max}
$\Delta\theta_{max}$	38.0					
	28.5	0.0	0.2	0.4	0.6	0.8
	19.0	0.0	0.4	0.8	1.2	1.6
	9.5	0.0	0.5	1.0	1.5	1.9
θ_s	0.0	0.0	0.7	1.4	2.1	2.7
	−11.0	0.0	0.5	1.0	1.5	1.8
	−22.0	0.0	0.3	0.6	0.9	1.2
	−33.0	0.0	0.3	0.6	0.9	1.1
$\Delta\theta_{min}$	−44.0					

Fig. 9. The BRDF of aluminum 6061-T6 for $\theta_i = 50°$, contained in the empirical look-up table.

Fig. 8. The measured BRDF of aluminum 6061-T6 for $\theta_i = 50°$.

Table 2
The four matrices of a CAD model facet.

Matrix	Name	Description	Example
V	Vertices	Vertex coordinates	$\begin{bmatrix} 0 & 0 & 0 \\ 0 & 0.5 & 0.5 \\ 0 & 0.5 & -0.5 \end{bmatrix}$
F	Facet	Vertex connection	$\begin{bmatrix} 1 & 2 & 3 \end{bmatrix}$
N	Normal	Unit vector	$\begin{bmatrix} 1 & 0 & 0 \end{bmatrix}$
C	Color	RGB values	$\begin{bmatrix} 1 & 0 & 0 \end{bmatrix}$

facet characteristics. Table 2 provides details about these matrices along with examples.

The red–green–blue (RGB) values are manually added to the STL files after their export from CAD software as this information is not natively incorporated. The material composition of a facet is defined by its RGB values.

3.4. An algorithm to calculate a spacecraft's overall sBRDF

Overall spacecraft sBRDF is determined using a geometric approach. The illumination and reflection geometry, $(\theta_i, \Delta\theta, \phi)$, of each of the model's triangular facets is first determined. The sBRDF of each facet's material, $f_r(\theta_i; \Delta\theta; \phi; \lambda)_{material}$, is obtained from its respective empirical look-up table using its geometry and RGB values by the following algorithm:

$$\text{RGB} \rightarrow \theta_i \rightarrow \Delta\theta \rightarrow \phi \rightarrow f_r(\theta_i; \Delta\theta; \phi; \lambda)_{material}$$
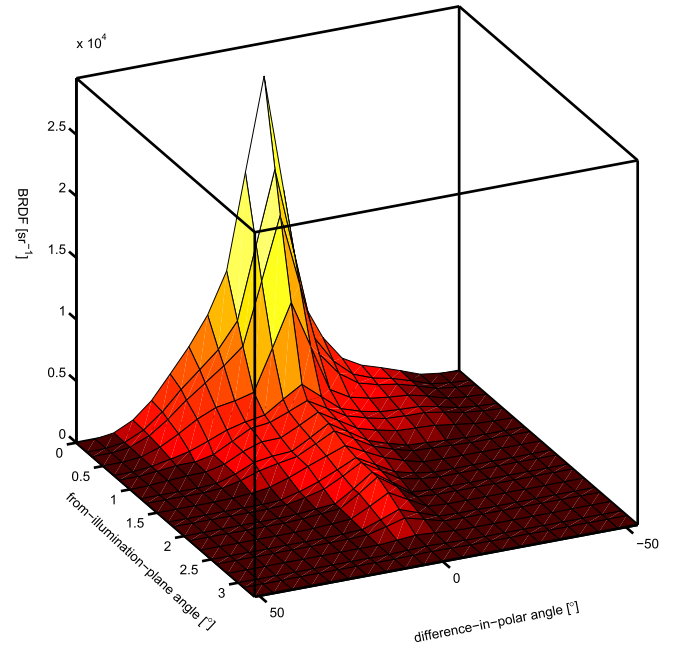
Eq. (3) shows how individual facet contribution to the overall sBRDF is calculated using the area of its orthogonal projection to the reflection direction, $a_{2D,facet}$.

$$f_r(\theta_i; \Delta\theta; \phi; \lambda)_{facet} = a_{2D,facet} \cdot f_r(\theta_i; \Delta\theta; \phi; \lambda)_{material} \quad [\text{sr}^{-1}] \quad (3)$$

The overall spacecraft sBRDF is calculated by calculating the sum of all facet sBRDFs and dividing the result by the total orthographic area of the spacecraft, as shown in Eq. (4):

$$f_r(\lambda)_{spacecraft} = \frac{\sum_{j=1}^{n} f_r(\theta_i; \Delta\theta; \phi; \lambda)_{facet,j}}{\sum_{j=1}^{n} a_{2D,facet,j}} \quad [\text{sr}^{-1}] \quad (4)$$

where n is the total number of triangular facets contributing to the spacecraft's reflectance. The summed sBRDF is divided by the total orthographic area of the contributing facets to normalize the result, ensuring that magnitude is independent of spacecraft size. The final product is the overall spacecraft sBRDF with respect to the illumination and reflection vectors.

4. Comparing quantities simulated using the spacecraft spectral reflectance model with those measured during the CanX-1 EM optical characterization experiment

The experiment set-up and procedure reproduced that of the ground truth characterization experiment by Bédard and Lévesque (2014). A CAD model of the CanX-1 EM, shown in Fig. 10, was constructed as the engineering CAD model could not be obtained. Scaled photographs were used to determine the dimensions of the CanX-1 EM's features.

The spacecraft CAD model, depicted in Fig. 11, was constructed with measurement specifications to half a millimeter. It is comprised of 698 triangular facets representing one of three materials: aluminum 6061-T6, Emcore TJPV cell, and LORD Aeroglaze® A276 white paint. The aluminum and solar cell, respectively in red and blue, were applied to the CAD model as these were the component materials of the spacecraft. The paint was applied to the remaining surfaces as its reflectance was spectrally uniform: its inclusion would not cause destructive interference with the spectral characteristics of the other materials.

Two observation scenarios were outlined within the characterization experiment. Simulations were developed to re-create these scenarios as closely as possible.

In the first simulation, the sBRDF of the CanX-1 EM's +X side was simulated for four specular reflection geometries: the illumination and reflection vectors, $\vec{v}_i$ and $\vec{v}_r$, were contained within the xy-plane with a phase angle separation of $\beta = 5°, 30°, 60°$, and $90°$. The angle between the +x-axis and $\vec{v}_i$ was equivalent to the angle between the +x-axis axis and $\vec{v}_r$. Fig. 12 provides a visual representation of this scenario.
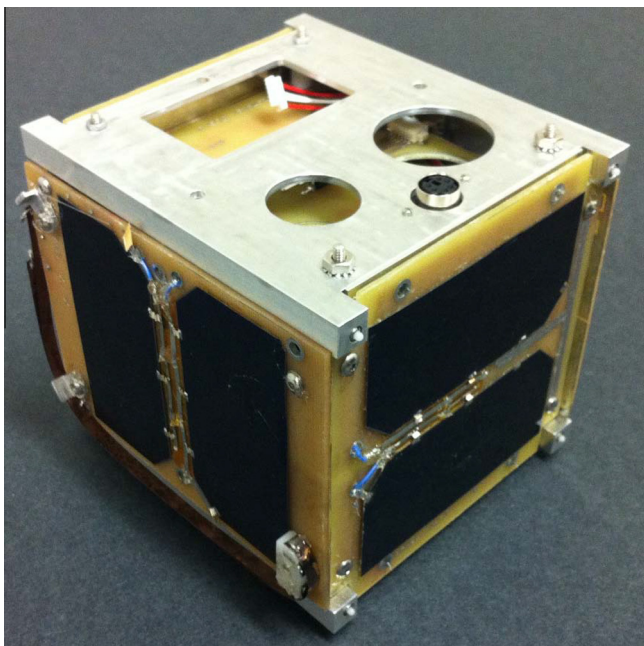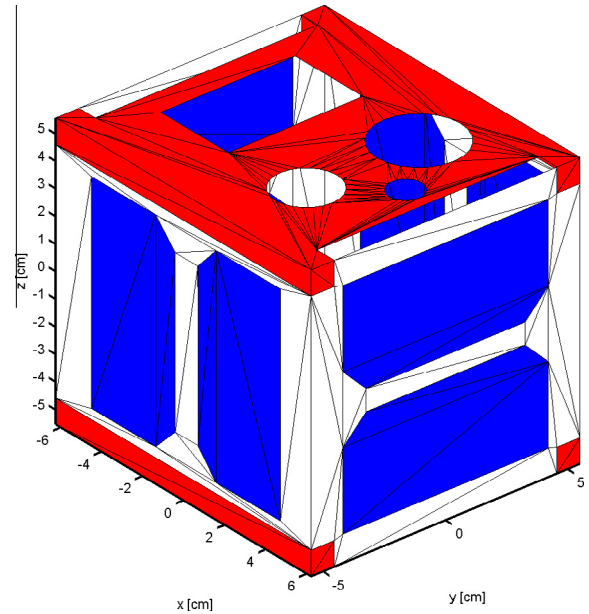

Fig. 11. The CanX-1 EM CAD model.

The second simulation started with the CAD model possessing an initial rotation of $25°$ about the $+z$-axis. It was then rotated $360°$ about the $-z$-axis in increments of $1°$. The sBRDF of the CanX-1 EM was simulated after each rotation increment and integrated to produce the spacecraft BRDF. The xy-plane contained $\vec{v}_i$ and $\vec{v}_r$ with a fixed-phase-angle separation of $\beta = 10°$, where the angle between the $+x$-axis and $\vec{v}_i$, and the angle between the $+x$-axis and $\vec{v}_r$, was $5°$. This scenario is presented in Fig. 13.

4.1. The simulated sBRDF and measured reflectance factor

The simulated sBRDF of the +X side of the CanX-1 EM for the first scenario is shown in Fig. 14, while the
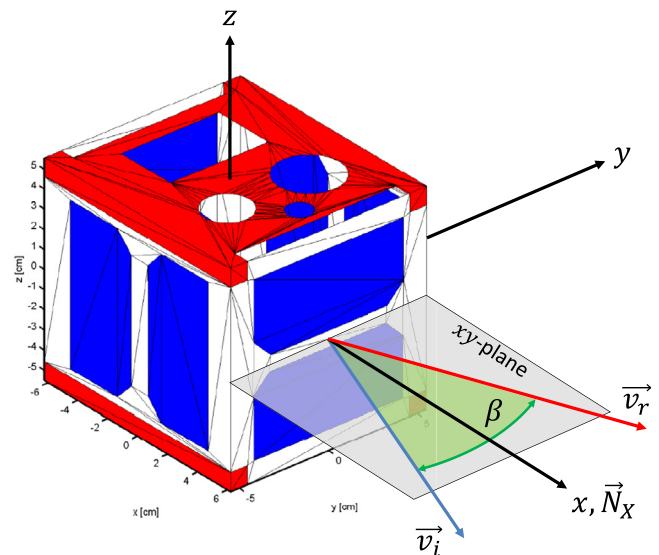

Fig. 10. The CanX-1 EM.

Fig. 12. The simulation scenario of the +X side of the CanX-1 EM.
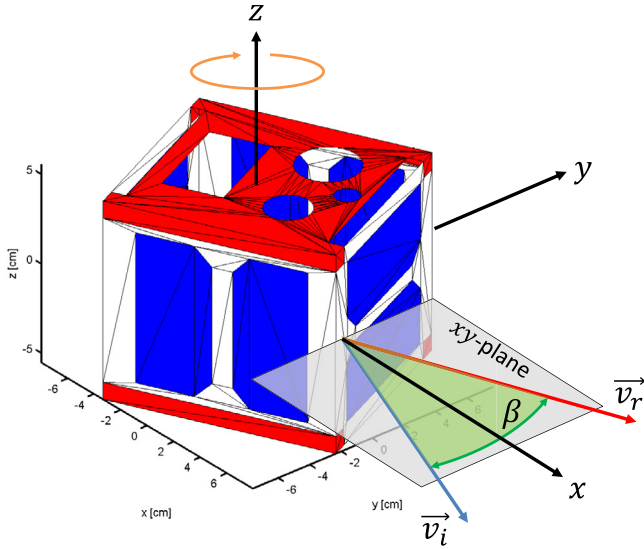
Fig. 13. The fixed-phase-angle simulation scenario of the CanX-1 EM.

Fig. 15. The measured reflectance factor of the +X side of the CanX-1 EM for four illumination and reflection geometries, for wavelength range 350–1000 nm (Bédard and Lévesque, 2014).

reflectance factor measured by Bédared et al. is shown in Fig. 15. Both the sBRDF and reflectance factor possess similar spectral characteristics including prominent features in the 600–800 nm range that shift towards shorter wavelengths with an increase in β. These features and their behavior are characteristic of Emcore TJPV cell, as demonstrated by Bédard et al. (2015). The presence of this material in both quantities was expected as the +X side of the CanX-1 EM is dominated by it.

While aluminum 6061-T6 is also present on the +X side of the spacecraft, its characteristic 800 nm absorption feature does not appear in the simulated sBRDF. This is because the sBRDF of the solar cell is greater than that of the aluminum for specular reflection geometries.
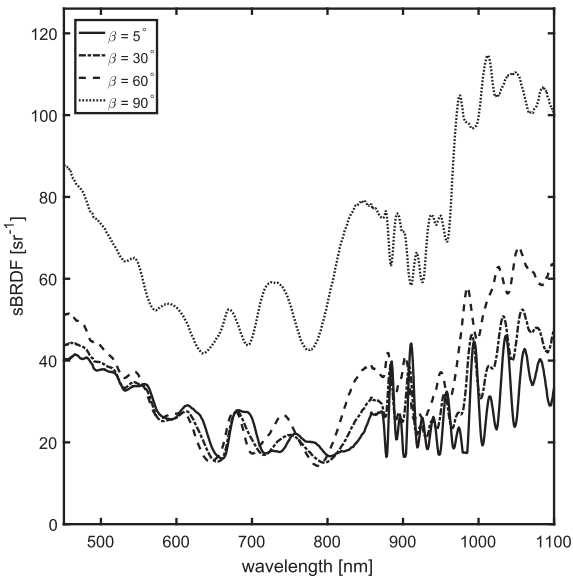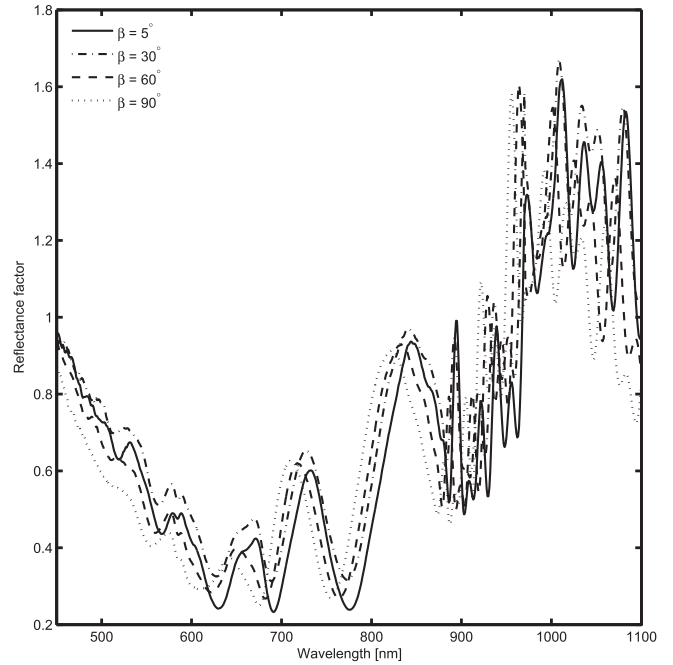
Fig. 16 shows how this characteristic feature becomes visible as reflection geometries move away from specular. Note that the y-axis of Fig. 16 is logarithmic to enable viewing the overall spacecraft sBRDF for this range of illumination and reflection geometries.

The magnitude of the sBRDF increases with an increase in β. This was also an expected phenomenon based on the conclusions reached by Bédard et al. This is not

Fig. 14. The simulated sBRDF of the +X side of the CanX-1 EM for four specular reflection geometries, for wavelength range 450–1100 nm.
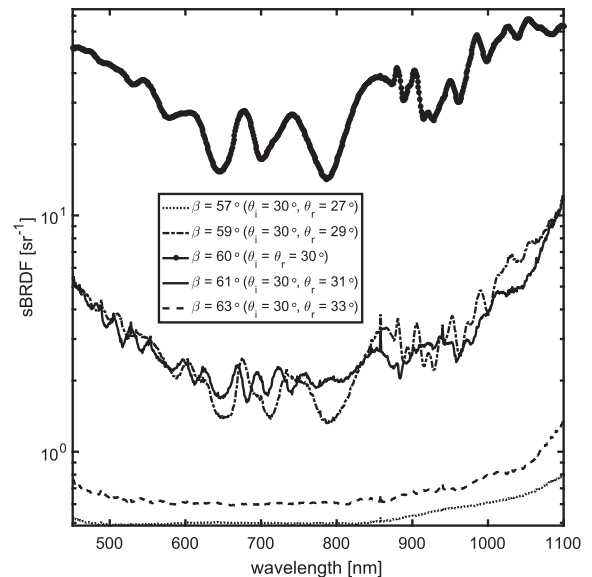

Fig. 16. The simulated sBRDF of the +X side of the CanX-1 EM for four reflection geometries that frame specular, for wavelength range 450–1100 nm.

demonstrated by the reflectance factor as it is essentially a normalization: its calculation removes information concerning the relationship between illumination and reflection geometry and reflectance magnitude.

While a quantitative comparison of the sBRDF and reflectance factor was not possible, one would undoubtedly indicate that the wavelength of the characteristic spectral features of each quantity are not equivalent. This is because the Emcore TJPV cells are not perfectly flat, nor are they flush to the surface of the spacecraft, as shown in Fig. 17. These characteristics were not represented by the CAD model.

4.2. The simulated BRDF and measured broadband photometric light curve

The simulated BRDF for the fixed-phase-angle simulation is shown in Fig. 18, while the broadband photometric light curve measured by Bédard et al. is shown in Fig. 19. Both the BRDF and light curve possess similar characteristics including a specular peak separation of 90° due to the cubic nature of the CanX-1 EM. Each peak presents a directional-diffuse base with a thin specular feature. This indicates that the spacecraft is composed of at least two materials, one of which is more specular than the other. The CanX-1 EM is known to possess Emcore TJPV cell and aluminum 6061-T6: Bédard et al. demonstrated that the solar cell is highly specular while the aluminum is more directional-diffuse. The discontinuities in the spacecraft BRDF, located to the left of all specular peaks, were present in the aluminum 6061-T6 empirical look-up table. They are the result of extrapolation of the sBRDF for
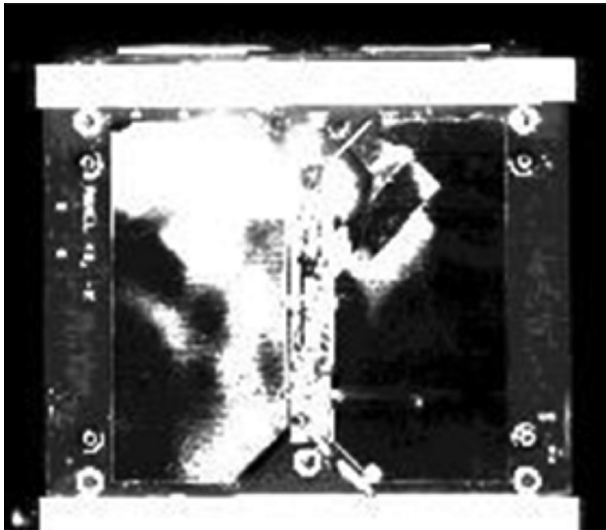

Fig. 17. An image of the CanX-1 EM clearly shows that the solar cells are not flat nor flush to the spacecraft surface; flat and flush solar cells would appear bright white in this image taken at specular. The "non-flatness" is demonstrated by the left cell, which exhibits specular reflection predominantly on the top right and none on the bottom left. The "non-flushness" can be seen when comparing the difference between the reflection of the left cell with that of the right (Bédard and Lévesque, 2014).
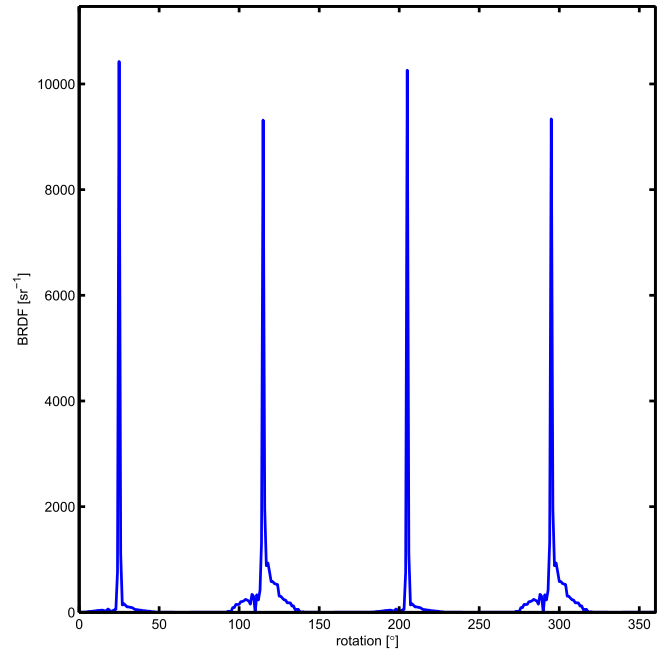

Fig. 18. The simulated BRDF of the CanX-1 EM, initially rotated 25° about the +z-axis, for a fixed-phase-angle scenario where the CAD model was rotated 360° about the −z-axis in increments of 1°, where $\vec{v}_i$ and $\vec{v}_r$ were fixed at $\beta = 10°$.
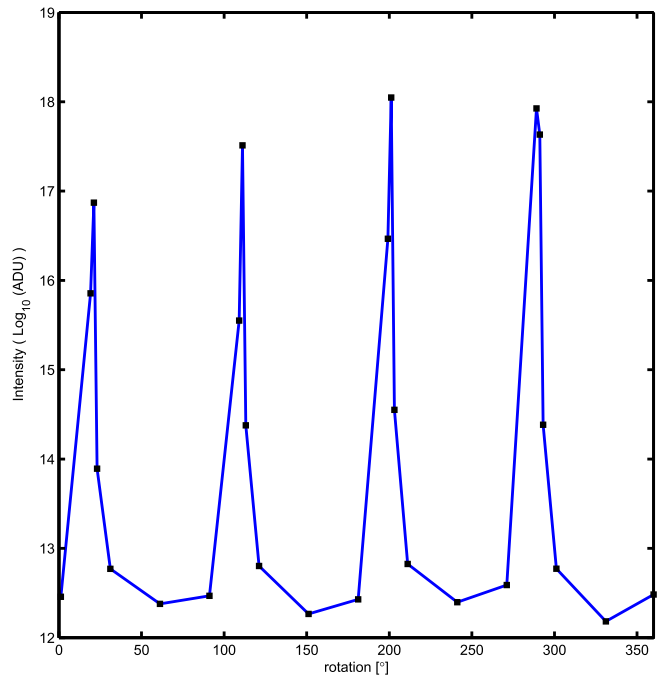

Fig. 19. The measured broadband photometric light curve of the CanX-1 EM, initially rotated 25° about the +z-axis, for a fixed-phase simulation where the CAD model was rotated 360° about the −z-axis in increments of 1°, where $\vec{v}_i$ and $\vec{v}_r$ were fixed at $\beta = 10°$ (Bédard and Lévesque, 2014).

illumination polar angles close to 0°, well below the smallest illumination angle that could be measured by the laboratory apparatus without obscuring the illumination beam, $\theta_i = 30°$. The look-up tables of Emcore TJPV cell

and LORD Aeroglaze® A276 white paint did not contain these discontinuities as the smallest measured θ_i was 10°.

The ordering of spacecraft sides observed during the simulation was +X→+Y→-X→-Y. The X-sides exhibited greater specular reflectance and lesser directional-diffuse reflectance when compared to the Y-sides. All four sides are known to possess the same coverage of Emcore TJPV cell; however, the solar cells on the X-sides are arrayed horizontally as opposed to vertically, as on the Y-sides. The horizontal orientation causes both cells to glint in unison, while they glint sequentially in the vertical orientation, resulting in specular peaks with lesser magnitude. The variation in directional-diffuse reflectance is due to the difference in aluminum 6061-T6 coverage: the X-sides have less aluminum than the Y-sides.

The broadband photometric light curve does not depict the same specularity as the BRDF. This is because measurements were made with a model rotation angle increment much greater than the 1° of the simulation, leaving uncertainty in the shape of the light curve. Additionally, the surfaces of the actual spacecraft are not perfectly flat, causing a wider model rotation angle range of specular reflection. Finally, the pattern seen in the alternating BRDF peak magnitudes, as well as the zero reflectance between the peaks, is not observed in the light curve. This is attributed to the non-flush Emcore TJPV cells and the presence of features and diffuse materials on the surface of the spacecraft that were not represented on the CAD model.

5. Conclusion

The validity of modeling a spacecraft's spectral reflectance as an overall sBRDF, generated using its CAD model and the empirical reflectance of homogeneous samples of its surface materials, has been demonstrated. While the comparison of simulated quantities with those from an actual optical ground truth characterization experiment was only qualitative, it is clear that this approach produces more valid results than the TASAT and DIRSIG systems based on the contents of published literature. The empirical material reflectance database developed as part of this approach is spectral in nature and complete for all illumination and reflection geometries, thus avoiding the dependency on theoretical BRDF models that have demonstrated a limited ability to model the spectral reflectance of different material types. Modeled spacecraft reflectance has also been demonstrated to be a function of illumination and reflection geometry using this approach, which was not consistently exhibited by the TASAT and DIRSIG systems.

This approach has three notable limitations. Primarily, the development of empirical look-up tables from sBRDF measurements requires extrapolation for illumination angles that can not be measured, due to physical constraints of laboratory apparatus. This extrapolation introduced discontinuities for more directional-diffuse

materials, as opposed to more specular ones. Investigation into the reduction of these negative extrapolation effects is required. Replacing the manual goniometer stage with a motorized one would enable full automation of the goniospectrometer system, allowing for many more measurements to be made, thereby reducing extrapolation error and removing the requirement for interpolation. Next, cautious use of CAD models as subjects should be observed as their physical features are arguably "perfect", whereas actual spacecraft possess minor imperfections that noticeably change their overall BRDF. A strategy to add these imperfections into the calculation of overall spacecraft reflectance requires development. Finally, spectral reflectance was assumed to be isotropic, which is not the case for more complex materials. Incorporation of anisotropic reflectance is an important consideration that must be made, especially when modeling more complex spacecraft.

Despite these limitations, it is clear that this approach to model spacecraft spectral reflectance shows more promise to simulate quantities that can be measured by optical telescopes than previous attempts to do so. The fact that it does so spectrometrically will eventually allow for the interpretation of the surface composition of unresolved objects for space surveillance characterization, a capability whose demand increases with the population of RSOs.

Acknowledgements

References

Abercromby, K., Okada, J., Guyote, M., Hamada, K., Barker, E., 2006. Comparisons of ground truth and remote spectral measurement of the FORMOSAT and ANDE spacecraft. In: Advanced Maui Optical and Space Surveillance Technologies Conference, URL: <http://ntrs.nasa.gov/archive/nasa/casi.ntrs.nasa.gov/20060024664.pdf>.

Bass, M., DeCusatis, C., Enoch, J., Lakshminarayanan, V., Li, G., Macdonald, C., Mahajan, V., Van Stryland, E., 2010. Handbook of Optics, Third Edition Volume II: Design, Fabrication and Testing, Sources and Detectors, Radiometry and Photometry, third ed. McGraw-Hill Inc, New York, NY, USA.

Bédard, D., 2013. Spectrometric Characterization of Artificial Earth-Orbiting Objects: Laboratory and Observational Experiments. The Royal Military College of Canada, Kingston, ON (Ph.D. thesis).

Bédard, D., Lévesque, M., 2014. Analysis of the CanX-1 engineering model spectral reflectance measurements. J. Spacecraft Rockets 51 (5), 1492–1504. http://dx.doi.org/10.2514/1.A32643.

Bédard, D., Lévesque, M., Wallace, B., 2011. Measurement of the photometric and spectral BRDF of small Canadian satellites in a controlled environment. In: Advanced Maui Optical and Space Surveillance Technologies Conference, URL: <http://pubs.drdc-rddc.gc.ca/BASIS/pcandid/www/engpub/DDW?W>.

Bédard, D., Wade, G.A., Abercromby, K., 2015. Laboratory characterization of homogeneous spacecraft materials. J. Spacecraft Rockets 52 (4), 1038–1056. http://dx.doi.org/10.2514/1.A33079.

Bédard, D., Wade, G.A., Jolley, A., 2014. Interpretation of spectrometric measurements of active geostationary satellites. In: Advanced Maui

Optical and Space Surveillance Technologies Conference. URL: <http://www.amostech.com/TechnicalPapers/2014/NROC/BEDARD.pdf>.

Bennett, D.A., Dank, J.A., Tyler, D.W., Gartley, M., Allen, D., 2014. SSA modeling and simulation with DIRSIG. In: Advanced Maui Optical and Space Surveillance Technologies Conference. URL: <http://www.amostech.com/TechnicalPapers/2014/Poster/BENNETT>.

Chaudhary, A.B., Payne, T., Gregory, S., Dao, P., 2011. Fingerprinting of non-resolved three-axis stabilized space objects using a two-facet analytical model. In: Advanced Maui Optical and Space Surveillance Technologies Conference. URL: <http://www.amostech.com/TechnicalPapers/2011/NROC/CHAUDHARY.pdf>.

del Monte, L., 2007. A European approach to Space Situational Awareness. European Space Agency, Brussels, Belgium, Tech. rep., URL: <http://swe.ssa.esa.int/DOCS/SWWT/m22/SSA-Space_Weather_Week.ppt>.

Duggin, M.J., Riker, J.F., Glass, W., Bush, K.A., Briscoe, D., Klein, M., Pugh, M.L., Engberg, B., 2008. Multi-spectral image analysis for improved space object characterization. In: Advanced Maui Optical and Space Surveillance Technologies Conference. No. ADA532030. URL: <http://oai.dtic.mil/oai/oai?verb=getRecord&metadataPrefix=html&identifier=ADA532030>.

Hall, D., 2010. Surface material characterization from non-resolved multi-band optical observations. In: Advanced Maui Optical and Space Surveillance Technologies Conference. URL: <http://www.amostech.com/TechnicalPapers/2010/NROC/Hall.pdf>.

Hall, D., Hamada, K., Kelecy, T., Kervin, P., 2012. Surface material characterization from non-resolved multi-band optical observations. In: Advanced Maui Optical and Space Surveillance Technologies Conference. URL: <http://www.amostech.com/TechnicalPapers/2012/NROC/HALL.pdf>.

Jolley, A., 2014. Multicolour Optical Photometry of Active Geostationary Satellites Using a Small Aperture Telescope (Master's thesis). The Royal Military College of Canada, Kingston, ON, URL: <http://espace.rmc.ca/handle/11264/121>.

Luu, K.K., Matson, C.L., Snodgrass, J., Giffin, S.M., Hamada, K., Lambert, J.V., 2003. Object characterization from spectral data. In: Advanced Maui Optical and Space Surveillance Technologies Conference. No. ADA423457. URL: <http://www.dtic.mil/cgi-bin/GetTRDoc?Location=U2&doc=GetTRDoc.pdf&AD=ADA423457>.

Maxwell, J., Beard, J., Weiner, S., Ladd, D., Ladd, S., 1973. Bidirectional reflectance model validation and utilization. Environmental Research Institute of Michigan (ERIM), Tech. Rep. AD0913816, URL: <http://www.dtic.mil/cgi-bin/GetTRDoc?Location=U2&doc=GetTRDoc.pdf&AD=AD0913816>.

NASA Orbital Debris Program Office, 2014. Monthly Number of Objects in Earth Orbit by Object Type. Orbital Debris Quarterly Newsletter 18, 10. URL: <http://orbitaldebris.jsc.nasa.gov/newsletter/pdfs/ODQNv18i1.pdf>.

Nicodemus, F.E., Richmond, J.C., Hsia, J.J., Ginsberg, I.W., Limperis, T., 1977. Geometrical Considerations and Nomenclature for Reflectance. UNT Digital Library, Washington, D.C., URL: <http://digital.library.unt.edu/ark:/67531/metadc70423/>.

Riker, J.F., Crockett, G.A., Brunson, R.L., 1992. Time-domain analysis simulation for advanced tracking. In: Proc. SPIE 1697, Acquisition, Tracking, and Pointing VI. vol. 1697. pp. 297–309. http://dx.doi.org/10.1117/12.138181.

Schaepman-Strub, G., Schaepman, M., Painter, T., Dangel, S., Martonchik, J., 2006. Reflectance quantities in optical remote sensing – definitions and case studies. Remote Sens. Environ. 103 (1), 27–42, URL: <http://www.sciencedirect.com/science/article/pii/S0034425706001167>.

Schott, J., Brown, S., Raqueño, R., Gross, H., Robinson, G., 1999. An advanced synthetic image generation model and its application to multi/hyperspectral algorithm development. Can. J. Remote Sens. 25 (2), 99–111. http://dx.doi.org/10.1080/07038992.1999.10874709.

Scott, R.L., Wallace, B., 2008. Satellite characterization using small aperture instruments at DRDC Ottawa. In: Advanced Maui Optical and Space Surveillance Technologies Conference. URL: <http://www.amostech.com/TechnicalPapers/2008/NROC/ScottWallace.pdf>.

Somers, P., 2011. Cylindrical RSO signatures, spin axis orientation and rotation period determination. In: Advanced Maui Optical and Space Surveillance Technologies Conference. URL: <http://www.amostech.com/TechnicalPapers/2011/NROC/SOMERS.pdf>.

Ward, G.J., 1992. Measuring and modeling anisotropic reflection. SIGGRAPH Comput. Graph. 26 (2), 265–272. http://dx.doi.org/10.1145/142920.134078.

Wells, G.J., Stras, L., Jeans, T., 2002. Canada's Smallest Satellite: The Canadian Advanced Nanospace eXperiment (CanX-1). In: Small Satellite Conference. URL: <http://digitalcommons.usu.edu/smallsat/2009/all2009/24/>.

Willison, A., 2015. Synthesizing Spacecraft Ground Truth Spectra Using Homogeneous Material Spectral BRDFs and Faceted CAD Models. The Royal Military College of Canada, Kingston, ON, Master's thesis, URL: <http://espace.rmc.ca/handle/11264/742>.